

Compression and ablation of the photo-irradiated cloud the Orion Bar*

Javier R. Goicoechea^a, J. Pety^{b,c}, S. Cuadrado^a, J. Cernicharo^a, E. Chapillon^{b,d,e},
A. Fuente^f, M. Gerin^{c,g}, C. Joblin^{h,i}, N. Marcelino^a and P. Pilleri^{h,i}

August 23, 2016

^aGrupo de Astrofísica Molecular. Instituto de Ciencia de Materiales de Madrid (CSIC).
Calle Sor Juana Ines de la Cruz 3, E-28049 Cantoblanco, Madrid, Spain.

^bInstitut de Radioastronomie Millimétrique, 300 rue de la Piscine, F-38406 Saint Mar-
tin d'Hères, France.

^cLERMA, Observatoire de Paris, CNRS UMR 8112, École Normale Supérieure, PSL
research university, 24 rue Lhomond, 75231, Paris Cedex 05, France.

^dUniversité de Bordeaux, LAB, UMR 5804, F-33270, Floirac, France.

^eCNRS, LAB, UMR 5804, F-33270 Floirac, France.

^fObservatorio Astronómico Nacional. Apartado 112, 28803, Alcalá de Henares, Spain.

^gSorbonne Universités, UPMC Université Paris 06, 75000, Paris, France.

^hUniversité de Toulouse, UPS-OMP, IRAP, 31028, Toulouse, France.

ⁱCNRS, IRAP, 9 Avenue du Colonel Roche, BP 44346, 31028 Toulouse, France.

*Manuscript accepted for publication in Nature. Submitted 13 February; accepted 8 June 2016.
This is the author's submitted version. Definitive version of the manuscript was published online by Nature
on 10 August 2016 (doi:10.1038/nature18957).

Abstract

The Orion Bar is the archetypal edge-on molecular cloud surface illuminated by strong ultraviolet radiation from nearby massive stars. Owing to the close distance to Orion (about 1,350 light-year), the effects of stellar feedback on the parental cloud can be studied in detail. Visible-light observations of the Bar[1] show that the transition between the hot ionised gas and the warm neutral atomic gas (the ionisation front) is spatially well separated from the transition from atomic to molecular gas (the dissociation front): about 15 arcseconds or 6,200 astronomical units (one astronomical unit is the Earth-Sun distance). Static equilibrium models[2, 3] used to interpret previous far-infrared and radio observations of the neutral gas in the Bar[4, 5, 6] (typically at 10-20 arcsecond resolution) predict an inhomogeneous cloud structure consisting of dense clumps embedded in a lower density extended gas component. Here we report one-arcsecond-resolution millimetre-wave images that allow us to resolve the molecular cloud surface. In contrast to stationary model predictions[7, 8, 9] there is no appreciable offset between the peak of the H_2 vibrational emission (delineating the H/H_2 transition) and the edge of the observed CO and HCO^+ emission. This implies that the H/H_2 and $\text{C}^+/\text{C}/\text{CO}$ transition zones are very close. These observations reveal a fragmented ridge of high-density substructures, photoablative gas flows and instabilities at the molecular cloud surface. The results suggest that the cloud edge has been compressed by a high-pressure wave that currently moves into the molecular cloud. The images demonstrate that dynamical and nonequilibrium effects are important for the cloud evolution.

The ALMA radiotelescope allows us to resolve the atomic to molecular gas transition at the edge of the Orion molecular cloud[10, 11, 12, 13] that is directly exposed to energetic radiation from the Trapezium stars (Fig. 1). The strong ultraviolet (UV) field drives a blister H II region (hot ionised hydrogen gas or H^+) that is eating its way into the parental molecular cloud. At the same time, flows of ionised gas stream away from the cloud surface at about 10 km s^{-1} (roughly the speed of sound c_{HII} at $T \approx 10^4 \text{ K}$)[10, 11]. The so-called photon-dominated or photo-dissociation region (PDR[14]; see sketch in Extended Data Fig. 1) starts at the H II region/cloud boundary where only far-UV radiation penetrates the “neutral” cloud, i.e. stellar photons with energies below 13.6 eV that cannot ionise H atoms but do dissociate molecules ($\text{H}_2 + \text{photon} \rightarrow \text{H} + \text{H}$), and ionise elements

such as carbon ($\text{C} + \text{photon} \rightarrow \text{C}^+ + \text{electron}$). Inside the PDR, the far-UV photon flux gradually decreases due to dust grain extinction and H_2 line absorption, and so does the gas and dust temperatures[14]. These gradients produce a layered structure with different chemical composition as one moves from the cloud edge to the interior[5, 13]. The ionised nebula (the H II region) can be traced by the visible-light emission from atomic ions (such as the $[\text{S II}]$ 6,731 Å electronic line). The ionisation front is delineated by the $[\text{O I}]$ 6,300 Å line of neutral atomic oxygen[15] (Fig. 1). Both transitions are excited by hot temperature collisions with electrons. Therefore, their intensities sharply decline as the electron abundance decreases by a factor of $\sim 10^4$ at the H^+/H transition layer. In Fig. 1b, the dark cavity between the ionisation front and the HCO^+ emitting zone is the neutral “atomic layer” ($x(\text{H}) > x(\text{H}_2) \gg x(\text{H}^+)$ where x is the species abundance with respect to H nuclei). This layer is very bright in mid-IR polycyclic aromatic hydrocarbon (PAH) emission, and cools via far-infrared O and C^+ emission lines[14]. Although most of the electrons are provided by the ionisation of C atoms (thus $x(e^-) \approx x(\text{C}^+) \approx 10^{-4}$)[14, 16], the gas is mainly heated by collisions with energetic (about 1 eV) electrons photo-ejected from small grains and PAHs[2, 14]. For the strong far-UV radiation flux impinging the Bar[3, 5], approximately 4.4×10^4 times the average flux in a local diffuse interstellar cloud[16], a gas density $n_{\text{H}} = n(\text{H}) + 2n(\text{H}_2)$ of $(4\text{--}5) \times 10^4 \text{ cm}^{-3}$ in the atomic layer is consistent with the observed separation between the ionisation and dissociation fronts[3, 4].

ALMA resolves the sharp edge where the HCO^+ and CO emission becomes intense (Fig. 2). These layers spatially coincide with the brightest peaks of H_2 vibrational emission (H_2^*) tracing the H/H_2 transition (Extended Data Fig. 2). Therefore, the H/H_2 and the $\text{C}^+/\text{C}/\text{CO}$ transition zones occur very close to each other. Static equilibrium models of a PDR with $n_{\text{H}} = (4\text{--}5) \times 10^4 \text{ cm}^{-3}$ predict, however, that the C^+/CO transition should occur deeper inside the molecular cloud because of the lower ionisation potential of C atoms (11.3 eV), and because CO may not self-shield from photodissociation as effectively as H_2 [4, 9, 14]. The spatial coincidence of several H_2^* and HCO^+ emission peaks shows that the formation of carbon molecules readily starts at the surface of the cloud (initiated by reactions of C^+ with H_2). This shifts the C^+/CO transition closer to the ionisation front and suggests that dynamical effects are important[17, 18].

To zero order, the CO $J=3\text{--}2$ line intensity peak ($T_{\text{peak}}^{\text{CO } 3\text{--}2}$ in K) is a measure of the gas temperature T in the molecular cloud ($\delta x > 15''$ in Fig. 2c, where δx is the distance to the ionisation front). The HCO^+ $J=4\text{--}3$ integrated line intensity ($W_{4\text{--}3}^{\text{HCO}^+}$ in K km s^{-1}), however, scales with the gas density n_{H} (see Methods and Extended Data Fig. 3). Although the $T_{\text{peak}}^{\text{CO } 3\text{--}2}$ image shows a relatively homogeneous temperature distribution, the $W_{4\text{--}3}^{\text{HCO}^+}$ image shows small-scale structure (Fig. 2a, 2b). In particular, ALMA resolves several bright HCO^+ emission peaks (filamentary substructures, some akin to globulettes) surrounding the dissociation front and roughly parallel to it. These substructures are sur-

rounded by a lower-density gas component, with $n_{\text{H}} \approx (0.5-1.0) \times 10^5 \text{ cm}^{-3}$, producing an extended (ambient) emission [4, 5]. The HCO^+ substructures (with a typical width of about $2'' \approx 4 \times 10^{-3} \text{ pc}$) are located at the molecular cloud edge, and are different from the bigger ($5''-10''$) condensations previously seen deeper inside the molecular cloud [6, 19].

To investigate the molecular emission stratification inside the cloud, we constructed averaged emission cuts perpendicular to the Bar. Three emission maxima are resolved in the $W_{4-3}^{\text{HCO}^+}$ crosscuts at roughly periodic separations of $\sim 5'' \approx 0.01 \text{ pc}$ (Fig. 2c). Excitation models show that the average physical conditions that reproduce the mean CO and HCO^+ intensities towards dissociation front (at $\delta x \approx 15''$) are $T \approx 200-300 \text{ K}$ and $n_{\text{H}} \approx (0.5-1.5) \times 10^6 \text{ cm}^{-3}$ (see Methods and Extended Data Fig. 3). Hence, the over-dense substructures have compression factors of $\sim 5-30$ with respect to the ambient gas component, and are submitted to high thermal pressures ($P/k = n_{\text{H}} \cdot T \approx 2 \times 10^8 \text{ K cm}^{-3}$). The three periodic maxima suggest that a high-pressure compression wave exists, and is moving into the molecular cloud. This wave may be associated with an enhanced magnetic field (several hundred μGauss ; see Methods).

In the very early stages of an H II region expansion upon molecular clouds, theory predicts that the ionisation and dissociation fronts are co-spatial (an *R*-type front [15, 20]). Soon after ($t < 10^3 \text{ yr}$), the expansion slows down and the dissociation front propagates ahead of the ionisation front and into the molecular cloud [16, 17]. The ionisation front changes to a *D*-type front (a compressive wave travels ahead of the ionisation front and the neutral gas becomes denser than the ionised gas [16, 20]). For a front advancing at a speed of $0.5-1.0 \text{ km s}^{-1}$ [17, 18], the observed separation between the ionisation and dissociation fronts in the Bar implies a crossing-time of 25,000-50,000 yr. For later times in the expansion phase, when t is several times the dynamical time (t_{dyn}) of the expanding H II region (the ratio of the initial H II region radius, so-called the Strömgren radius, and the speed of sound c_{HII}), the compressive wave slowly enters into the molecular cloud ($t_{\text{dyn}} \approx 0.2 \text{ pc per } 10 \text{ km s}^{-1} \approx 20,000 \text{ yr}$ for the Bar) [21, 22]. Observational evidences of such dynamical effects are scarce.

In the compressed layers suggested by ALMA (where δx is between $7''$ and $30''$ in Fig. 2a), the distribution of gas densities follows a relatively narrow log-normal distribution (Fig. 2d). This is consistent with magneto-hydrodynamic simulations of non-gravitating turbulent clouds [23, 24]. When the entire observed field is analysed, the shape of the distribution is closer to a double-peaked log-normal distribution. This resembles specific simulations in which the cloud compression is induced by the expansion of the ionised gas [24, 25] (and not by a strong turbulence). Searching for additional support to this scenario, we investigated the degree of turbulence and compared the different contributions to the gas pressure in the PDR (Extended Data Table 1). The inferred non-thermal

(turbulent) velocity dispersion, about 1 km s^{-1} , results in a moderate Mach number of $\lesssim 1$ (the ratio of the turbulent velocity dispersion to the local speed of sound), i.e. only a gentle level of turbulence. The thermal pressure exerted by the H II region at the H^+/H interface[1] is several times higher than the turbulent and thermal pressures in the ambient molecular cloud. These pressure differences, together with the detection of over-dense substructures close to the cloud edge, agree with the UV radiation-driven compression scenario[25, 26]. Whether these substructures can be the seed of future star-forming clumps (e.g. by merging into massive clumps) is uncertain[22, 27]. At least presently, gravitational collapse is not apparent from their density distribution (no high-density power-law tail[24, 25]). Indeed, their estimated masses (less than about 0.005 M_\odot) are much lower than the mass needed to make them gravitationally unstable. Even so, the increased UV-shielding produced by the ridge of high-density substructures likely contributes to protect the molecular cloud against photo-destruction for longer times.

The ALMA images also show CO emission ripples[28] along the molecular cloud surface (undulations separated by less than about $5'' \approx 0.01 \text{ pc}$ in Fig. 2b) indicative of instabilities at the dissociation front. Such small-scale corrugations resemble the “thin-shell” instability produced by the force imbalance between thermal (isotropic) and ram pressure (parallel to the flow)[29]. Characterising these interface instabilities in detail would require new magneto-hydrodynamic models including: i) mesh-resolutions that are well below the $0.1\text{--}0.01 \text{ pc}$ scales achieved in current simulations[25], and ii) include neutral gas thermochemistry.

Finally, ALMA reveals fainter HCO^+ and CO emission in the atomic layer (HCO^+ globulettes and plume-like CO features at $\delta x < 15''$, see Fig. 2a, 2b). The dense gas HCO^+ emission structures must have survived the passage of the dissociation front[30], whereas the CO plumes may trace either warm CO that *in situ* reforms in the atomic layer, or molecular gas that advects or photoablates[28] from the molecular cloud surface. In the latter case, the pressure difference between the compressed molecular layers and the lower density atomic layer would favour such a flow. Interestingly, molecular line profiles from the plumes typically show two velocity components, one of them identical to that of gas from inside the Bar (Extended Data Fig. 4). This kinematic association supports the presence of photoablative flows through the atomic layer, and overall agrees with the suggested role of dynamical and non-equilibrium effects in UV-irradiated clouds.

References

- [1] Walmsley, C. M., Natta, A., Oliva, E. & Testi, L. The structure of the Orion Bar. *Astron. Astrophys.* **364**, 301–317 (2000).

- [2] Tielens, A. G. G. M. & Hollenbach, D. J. Photodissociation regions. I: basic model. *Astrophys. J.* **291**, 722–754 (1985).
- [3] Andree-Labsch, S., Ossenkopf, V. & Röllig, M. 3D modelling of clumpy PDRs: understanding the Orion Bar stratification. *Preprint at <http://arxiv.org/abs/1405.5553>* (2014).
- [4] Tielens, A. G. G. M. *et al.* Anatomy of the photodissociation region in the Orion Bar. *Science* **262**, 86–89 (1993).
- [5] Hogerheijde, M. R., Jansen, D. J., & van Dishoeck, E. F. Millimeter and submillimeter observations of the Orion Bar. 1: physical structure. *Astron. Astrophys.* **294**, 792–810 (1995).
- [6] Young Owl, R. C. *et al.* HCN and HCO⁺ images of the Orion Bar photodissociation region. *Astrophys. J.* **540**, 886–906 (2000).
- [7] Sternberg, A. & Dalgarno, A. Chemistry in dense photon-dominated regions. *Astrophys. J. Suppl. Ser.* **99**, 565–607 (1995).
- [8] Le Petit, F. *et al.* A model for atomic and molecular interstellar gas: The Meudon PDR code. *Astrophys. J. Suppl. Ser.* **164**, 506–529 (2006).
- [9] Röllig, M. *et al.* A photon dominated region code comparison study. *Astron. Astrophys.* **467**, 187–206 (2007).
- [10] Genzel, R. & Stutzki, J. The Orion molecular cloud and star-forming region. *Annu. Rev. Astron. Astrophys.* **27**, 41–85 (1989).
- [11] Goicoechea, J. R. *et al.* Velocity-resolved [C II] emission and [C II]/FIR mapping along Orion with Herschel. *Astrophys. J.* **812**, 75 (2015).
- [12] O’Dell, C. R. The Orion Nebula and its associated population. *Annu. Rev. Astron. Astrophys.* **39**, 99–136 (2001).
- [13] van der Werf, P. P. *et al.* Tearing the veil: interaction of the Orion Nebula with its neutral environment. *Astrophys. J.* **762**, 101 (2013).
- [14] Hollenbach, D. J. & Tielens, A. G. G. M. Photodissociation regions in the interstellar medium of galaxies. *Rev. Mod. Phys.* **71**, 173–230 (1999).
- [15] Weillbacher, P. M. *et al.* A MUSE map of the central Orion Nebula (M42). *Astron. Astrophys.* **582**, A114 (2015).
- [16] Draine, B. T. Physics of the Interstellar and Intergalactic Medium. *Princeton Univ. Press* (2011).

- [17] Bertoldi, F. & Draine, B. T. Nonequilibrium photodissociation regions: ionization-dissociation fronts. *Astrophys. J.* **458**, 222–232 (1996).
- [18] Störzer, H. & Hollenbach, D. J. Nonequilibrium photodissociation regions with advancing ionization fronts. *Astrophys. J.* **495**, 853–870 (1998).
- [19] Lis, D. C. & Schilke, P. Dense molecular clumps in the Orion Bar photon-dominated region. *Astrophys. J.* **597**, L145–L148 (2003).
- [20] Spitzer, L. Physical Processes in the Interstellar Medium. *Wiley* (1978).
- [21] Hill, J. K. & Hollenbach, D. J. Effects of expanding compact H II regions upon molecular clouds: molecular dissociation waves, shock waves, and carbon ionization. *Astrophys. J.* **225**, 390–404 (1978).
- [22] Hosokawa, T. & Inutsuka, S.-i. Dynamical expansion of ionization and dissociation front around a massive star. II: on the generality of triggered star formation. *Astrophys. J.* **646**, 240–257 (2006).
- [23] Hennebelle, P. & Falgarone, E. Turbulent molecular clouds. *Astron. Astrophys. Rev.* **20**, 55 (2012).
- [24] Federrath, C. & Klessen, R. S. On the star formation efficiency of turbulent magnetized clouds. *Astrophys. J.* **763**, 51 (2013).
- [25] Tremblin, P. *et al.* 3D simulations of globule and pillar formation around H II regions: turbulence and shock curvature. *Astron. Astrophys.* **546**, A33 (2012).
- [26] Gorti, U. & Hollenbach, D. J. Photoevaporation of clumps in photodissociation regions. *Astrophys. J.* **573**, 215–237 (2002).
- [27] Elmegreen, B. G. & Lada, C. J. Sequential formation of subgroups in OB associations. *Astrophys. J.* **2014**, 725–741 (1977).
- [28] Berné, O. *et al.* Waves on the surface of the Orion molecular cloud. *Nature* **466**, 947–949 (2010).
- [29] García-Segura, G. & Franco, J. & From ultracompact to extended H II regions. *Astrophys. J.* **469**, 171–188 (1996).
- [30] Lefloch, B. & Lazareff, B. Cometary globules. 1: formation, evolution and morphology. *Astron. Astrophys.* **289**, 559–578 (1994).

Acknowledgements We thank the ERC for support under grant ERC-2013-Syg-610256-NANOCOSMOS. We also thank Spanish MINECO for funding support under grants CSD2009-00038 and AYA2012-32032. This work was in part supported by the French CNRS program “Physique et Chimie du Milieu Interstellaire”. We thank P. Schilke and D. Lis for sharing their IRAM-PdBI observations of the H^{13}CN $J=1-0$ condensations inside the Bar, and M. Walmsley for sharing his H_2 $v=1-0$ $S(1)$ and O I $1.3\,\mu\text{m}$ infrared images. ALMA is a partnership of ESO (representing its member states), NSF (USA) and NINS (Japan), together with NRC (Canada), NSC and ASIAA (Taiwan), and KASI (Republic of Korea), in cooperation with the Republic of Chile. The Joint ALMA Observatory is operated by ESO, AUI/NRAO and NAOJ. This paper makes use of observations obtained with the IRAM-30m telescope. IRAM is supported by INSU/CNRS (France), MPG (Germany), and IGN (Spain).

Competing Interests The authors declare that they have no competing financial interests.

Author contributions J. R. G. was the PI of the ALMA project. He led the scientific analysis, modelling and wrote the manuscript. J. P. and E. C. carried out the ALMA data calibration and data reduction. S. C. and N. M. carried out the single-dish maps observations with the IRAM-30m telescope. All authors participated in the discussion of results, determination of the conclusions and revision of the manuscript.

Author information The authors declare no competing financial interests. Correspondence and requests for materials should be addressed to jr.goicoechea@icmm.csic.es. This paper makes use of the following ALMA data: ADS/JAO.ALMA#2012.1.00352.S.

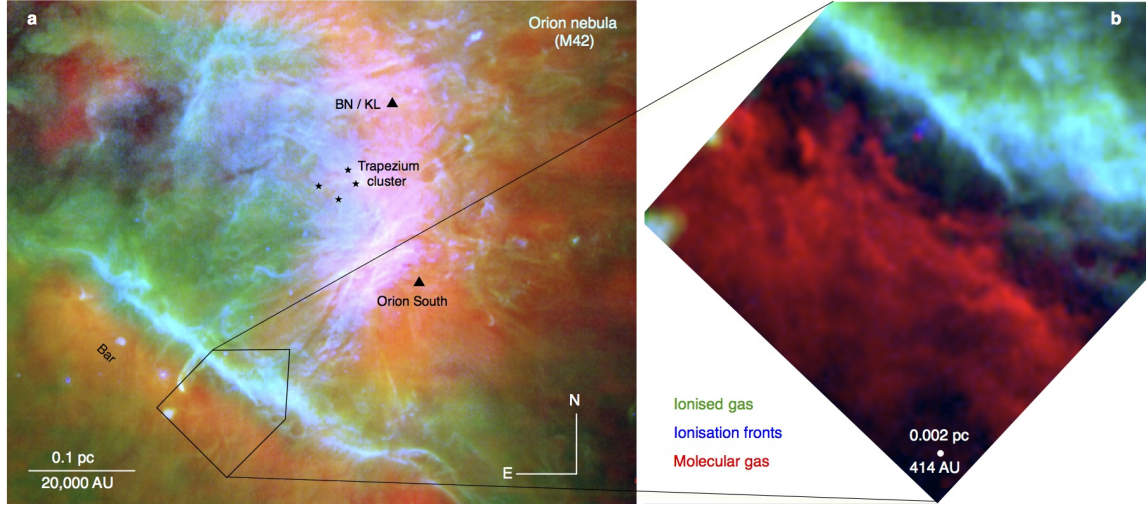


Figure 1: Multiphase view of the Orion nebula and molecular cloud. **a**, Overlay of the HCO^+ $J=3-2$ emission (red) tracing the extended Orion molecular cloud. The hot ionised gas surrounding the Trapezium stars is shown by the $[\text{S II}]$ $6,731 \text{ \AA}$ emission (green). The interfaces between the ionised and the neutral gas, the ionisation fronts, are traced by the $[\text{O I}]$ $6,300 \text{ \AA}$ emission (blue), both lines imaged with VLT/MUSE[15]. The size of the image is $\sim 5.8' \times 4.6'$. **b**, Close-up of the Bar region imaged with ALMA in the HCO^+ $J=4-3$ emission (red). The black-shaded region is the atomic layer.

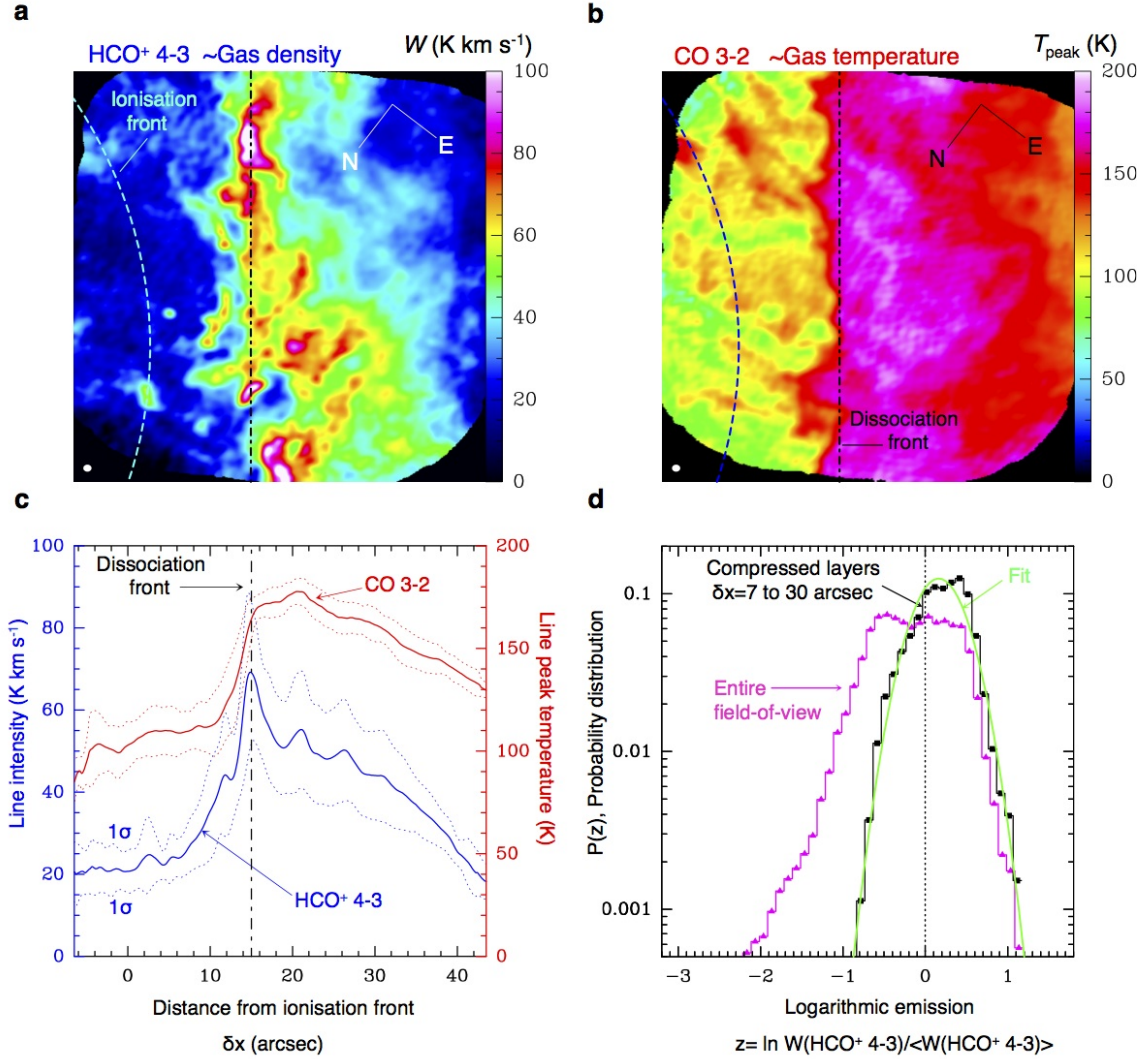


Figure 2: ALMA images of the Orion Bar. a, HCO⁺ $J=4-3$ line integrated intensity. b, CO $J=3-2$ line peak. Compared to Fig. 1, images a and b have been rotated by 127.5° anticlockwise to bring the incident UV radiation from left (see sketch in Extended Fig. 1). The dashed curve and the vertical dotted-dashed line delineate the ionisation and dissociation fronts respectively[1]. c, Vertically-averaged intensity cuts perpendicular to the Bar in $W_{4-3}^{\text{HCO}^+}$ (blue curve) and $T_{\text{peak}}^{\text{CO } 3-2}$ (red curve). d, Probability distribution of $W_{4-3}^{\text{HCO}^+}$ (proportional to the gas density) in the observed field (magenta triangles) and in the compressed layers (black squares).

Methods

ALMA interferometric and IRAM-30m single-dish observations

ALMA Cycle-1 observations of the Bar were carried out using twenty-seven 12 m antennae in band 7 at 345.796 GHz (CO $J=3-2$) and 356.734 GHz (HCO⁺ $J=4-3$). The observations consisted of a 27-pointing mosaic centred at $\alpha(2000) = 5^h35^m20.6^s$; $\delta(2000) = -05^\circ25'20''$. The total field-of-view (FoV) is $58'' \times 52''$. Baseline configurations from ~ 12 to ~ 444 m were used (C32-3 antennae configuration). Lines were observed with correlators providing ~ 500 kHz resolution ($\delta v \approx 0.4$ km s⁻¹) over a 937.5 MHz bandwidth. The ALMA 12 m array total observation time was ~ 2 h. ALMA executing blocks were first calibrated in the CASA software (version 4.2.0) and then exported to GILDAS. In order to recover the large-scale extended emission filtered out by the interferometer, we used fully sampled single-dish maps as “zero-” and “short-spacings”. Maps were obtained with the IRAM-30m telescope (Pico Veleta, Spain) using the EMIR330 receiver under excellent winter conditions (< 1 mm of precipitable water vapour). On-The-Fly (OTF) scans of a $170'' \times 170''$ region were obtained along and perpendicular to the Orion Bar. The beam full-width at half maximum power (FWHM) at 350GHz is $\sim 7''$. The GILDAS/MAPPING software was used to create the short-spacing visibilities[31] not sampled by ALMA. These visibilities were merged with the interferometric observations. Each mosaic field was imaged and a dirty mosaic was built. The dirty image was deconvolved using the standard Högbom CLEAN algorithm and the resulting cubes were scaled from Jy/beam to brightness temperature scale using the synthesized beam size of $\sim 1''$. This is a factor of ~ 9 higher resolution than previous interferometric observations of the HCO⁺ $J=1-0$ line towards the Bar[6]. The achieved rms noise is ~ 0.4 K per 0.4 km s⁻¹ channel, with an absolute flux accuracy of $\sim 10\%$. The resulting images are shown in Fig. 1b and 2, and in Extended Data Fig. 2. Finally, the large-scale HCO⁺ $J=3-2$ (267.558 GHz) OTF map shown in Fig. 1a was taken with the multi-beam receiver HERA, also at the IRAM-30m telescope. The spectral and angular resolutions are ~ 0.4 km s⁻¹ and $9''$ (FWHM) respectively. The final images were generated using the GILDAS/GREG software.

Saturation and extinction corrections for the near-infrared image

To better understand the spatial distribution of the H₂ $v=1-0$ $S(1)$ line emission at $\lambda=2.12$ μ m (H₂^{*}) presented in ref.[1] and shown in Extended Data Fig. 2, we note two effects that determine the resulting emission morphology. First, there is a bright star in the line of sight towards the Bar (Θ^2 AOri at $\alpha(2000)=5^h35^m22.9^s$; $\delta(2000)=-05^\circ24'57.8''$) that saturates the near-IR detectors in a slit of $\sim 4''$ -width parallel to the Bar (roughly between $\delta x = 19''$ and $23''$ in our rotated images). Hence, no H₂^{*} data is shown in this range. Therefore, the layers with H₂ vibrational emission are wider than what Extended Data Fig. 2 might suggest, and more H₂^{*} emission peaks can coincide with HCO⁺ peaks in the blanked $\delta x = 19'' - 23''$ region. Older, lower-angular and -spectral resolution near-IR images do

show[32] that the H_2^* emission extends out to $\delta x \simeq 20''$. Second, dust extinction (due to foreground dust in Orion’s Veil and also due to dust in the Bar itself) may affect the apparent morphology of the near-IR images. Such effects are often neglected[1, 32, 33] and are not included in Extended Data Fig. 2. The extinction towards the Bar produced by the Veil is not greater than about 2 mag[34]. Adopting a dust reddening appropriate to Orion[11, 35], $R_V=A_V/E(\text{B-V})=5.5$, and the A_K/A_V extinction law in ref.[35], we estimate that the H_2^* emission lines would only be a factor of $\sim 30\%$ brighter if foreground extinction corrections are taken into account. An additional magnitude of extinction due to dust in the atomic layer of the Bar itself, results in a line intensity increase of $\sim 50\%$. Therefore, minor morphological differences between the near-IR and millimetre-wave images can reflect a small-scale or patchy extinction differences in the region[1].

Excitation and radiative transfer models for CO and HCO^+

In order to estimate the physical conditions of the HCO^+ emitting gas near the dissociation front we run a grid of non-local, non-LTE excitation and radiative transfer (Monte Carlo) models. This approach allows us to explore different column densities, gas temperatures and densities. Compared to most PDR models (using local escape probability approximations) our models take radiative pumping, line trapping and opacity broadening into account. This allows for the treatment of optically thick lines (see the Appendix in ref.[36] for code details and benchmarking tests). Our models use the most recent inelastic collisional rates of HCO^+ with H_2 and with electrons, and of CO with both H_2 and H . The electron density, n_e , can be an important factor in the collisional excitation of molecular cations in FUV-illuminated gas. For HCO^+ , collisions with electrons start to contribute above $n_e > 10 \text{ cm}^{-3}$ (or $n_{\text{H}} > 10^5 \text{ cm}^{-3}$ if most of the electrons are provided by carbon atom ionisation). In PDRs, collisions of molecules with H atoms can also contribute because the molecular gas fraction, $f=2n(\text{H}_2)/n_{\text{H}}=2n(\text{H}_2)/[n(\text{H})+2n(\text{H}_2)]$, is not 1 (fully molecular gas). We adopted $f=0.8$ and varied x_e between 0 and 10^{-4} . The H_2 ortho-to-para ratio was computed for each gas temperature T . Radiative excitation by the cosmic microwave background ($T_{\text{CMB}}=2.7 \text{ K}$) and by the FIR dust continuum in the Bar[37] (simulated by optically thin thermal emission at $T_{\text{dust}} = 55 \text{ K}$) were also included.

Column densities of $N(\text{HCO}^+)=(5\pm 1)\times 10^{13} \text{ cm}^{-2}$ and $N(\text{CO})=(1.0\pm 0.5)\times 10^{18} \text{ cm}^{-2}$ were estimated utilizing information from our IRAM-30m telescope line-survey towards the dissociation front[38]. This includes several HCO^+ , H^{13}CO^+ , HC^{18}O^+ and C^{18}O rotational lines in the estimation (the quoted dispersions in the column densities reflect the uncertainty obtained from least square fits to rotational population diagrams). They are consistent with previous observations in the region[5, 6]. Radiative transfer models were run for $N(\text{HCO}^+)=5\times 10^{13} \text{ cm}^{-2}$, $N(\text{CO})=1.0\times 10^{18} \text{ cm}^{-2}$, and $N_{\text{H}}=N(\text{H})+2N(\text{H}_2)\approx 2\times 10^{22} \text{ cm}^{-2}$ (equivalent to $A_V\approx 7 \text{ mag}$ for the dust properties in Orion). This results in $x(\text{HCO}^+)\approx (2-3)\times 10^{-9}$ and $x(\text{CO})\approx (2.5-7.5)\times 10^{-5}$ abundances. In addition, the $\text{HCO}^+/\text{H}^{13}\text{CO}^+$ column density ratios derived from single-dish observations are similar to the $^{12}\text{C}/^{13}\text{C}=67$

isotopic ratio in Orion[39]. Thus, the H^{12}CO^+ lines are not very opaque ($\tau_{\text{line}} \simeq 2$) otherwise the observed $\text{HCO}^+/\text{H}^{13}\text{CO}^+$ line intensity ratios would be considerably smaller. A non-thermal (turbulent) velocity dispersion σ_{nth} of about 1 km s^{-1} reproduces the observed line widths. A similar value, $\sigma_{\text{nth}} \simeq 1.0\text{--}1.5 \text{ km s}^{-1}$, is inferred directly from the observed line profiles ($\sigma_{\text{nth}}^2 = \sigma_{\text{obs}}^2 - \sigma_{\text{th}}^2$, with $\Delta v_{\text{FWHM}} = 2\sqrt{2\ln 2} \sigma_{\text{obs}} \approx 3.0 \pm 0.5 \text{ km s}^{-1}$ and $T = 300 \text{ K}$). Hence, opacity broadening plays a minor role. The dispersion σ_{nth} is similar or lower than the local speed of sound at $T = 100\text{--}300 \text{ K}$ ($c_{\text{PDR}} = (kT/m)^{1/2} = 1.0\text{--}1.7 \text{ km s}^{-1}$, where m is the mean mass per particle). This results in moderate Mach numbers ($M = \sigma_{\text{nth}}/c_{\text{PDR}} \lesssim 1$).

Extended Data Fig. 3 shows model predictions for the CO $J=3\text{--}2$ line intensity peak, $T_{\text{peak}}^{\text{CO } 3-2}$ (upper left panel), and HCO^+ $J=4\text{--}3$ line integrated intensity, $W_{4-3}^{\text{HCO}^+} = \int T_B dv$ (K km s^{-1}), for different T and n_{H} values. For optically thick lines ($\tau_{\text{line}} \gg 1$), $T_{\text{peak}}^{\text{CO } 3-2}$ provides a good measure of T_{ex} , with $T_{\text{peak}} \approx J(T_{\text{ex}}) = E_{\text{up}}/k (e^{E_{\text{up}}/k T_{\text{ex}}} - 1)^{-1}$. In addition, for low critical density (n_{cr}) transitions such as the low- J CO transitions, lines are close to thermalisation at densities above $\sim 10^4 \text{ cm}^{-3}$, thus $T_{\text{ex}} \rightarrow T$ (with $n_{\text{cr}} = A_{ij}/\gamma_{ij}$, where A_{ij} is the Einstein coefficient for spontaneous emission and γ_{ij} is the collisional de-excitation rate coefficient).

In this case, $T_{\text{peak}}^{\text{CO } 3-2}$ is a good thermometer of the $\tau_{\text{CO } 3-2} \gg 1$ emitting layers. The HCO^+ $J=4\text{--}3$ line, however, has much higher critical densities ($n_{\text{cr}, \text{H}_2} > 5 \times 10^6 \text{ cm}^{-3}$ and $n_{\text{cr}, \text{e}} \simeq 10^3 \text{ e cm}^{-3}$). For $n_{\text{H}} < 2n_{\text{cr}, \text{H}_2}/\tau_{\text{line}}$ (sub-thermal excitation), the integrated line intensity $W_{4-3}^{\text{HCO}^+}$ is approximately linearly proportional to $N(\text{HCO}^+) = x(\text{HCO}^+) \cdot n_{\text{H}} \cdot l$ even if the line is moderately thick. PDR models[6, 7] and CO observations respectively show that $x(\text{HCO}^+)$ and T do not change significantly in the PDR layers around the H_2^* emission peaks (between $A_V \approx 1$ and 2 mag). In a nearly edge-on PDR, the spatial length along the line of sight l does not change much either. We compute that for the inferred T and $N(\text{HCO}^+)$ values in the region, the integrated line intensity $W_{4-3}^{\text{HCO}^+}$ is proportional to density in the $n_{\text{H}} = 10^{4\text{--}6} \text{ cm}^{-3}$ range (the correlation coefficient is $r \simeq 0.98$ for models with $x_{\text{e}} = 0$ and 10^{-4}). Moreover, $W_{4-3}^{\text{HCO}^+}$ still increases with density up to several 10^6 cm^{-3} ($r \simeq 0.94$). This reasoning justifies the use of $W_{4-3}^{\text{HCO}^+}$ as a proxy for n_{H} in the region.

Average physical conditions in the compressed structures

The physical conditions that reproduce the mean CO $J=3\text{--}2$ line peak and HCO^+ $J=4\text{--}3$ integrated line intensity towards the compressed structures at $\delta x \simeq 15''$ ($T_{\text{peak}}^{\text{CO } 3-2} = 164 \pm 10 \text{ K}$ and $W_{4-3}^{\text{HCO}^+} = 69 \pm 18 \text{ K km s}^{-1}$) are $T = 200\text{--}300 \text{ K}$ and $n_{\text{H}} = (1.0 \pm 0.5) \times 10^6 \text{ cm}^{-3}$ (Extended Data Fig. 3). This implies high thermal pressures, $P_{\text{th, comp}}/k = n_{\text{H}} \cdot T \approx (1.0\text{--}4.5) \times 10^8 \text{ K cm}^{-3}$. The brightest HCO^+ emission peaks (with $W_{4-3}^{\text{HCO}^+} \simeq 100 \text{ K km s}^{-1}$, Fig. 2a) likely correspond to specific density enhancements. For the range of column densities and physical conditions at $\delta x \simeq 15''$, the T uncertainty is determined by the lack of higher- J CO lines, observed at high-angular resolution, to better constrain T from models. The range of estimated gas densities is dominated by the dispersion ($\sim 25\%$) of the mean $W_{4-3}^{\text{HCO}^+}$.

The above conditions suggest that the cloud edge contains substructures that are denser than the atomic layer ($n_{\text{H}}=(4-5)\times 10^4 \text{ cm}^{-3}$) [3, 4] and denser than the ambient molecular cloud ($n_{\text{H}}=(0.5-1.0)\times 10^5 \text{ cm}^{-3}$) [5]. The equivalent length of the substructures is small, $l=N_{\text{H}}/n_{\text{H}}\approx(4-12)\times 10^{-3} \text{ pc}$ ($\approx 2''-6''$ at the distance to Orion, thus consistent with their apparent size in the ALMA image). The mass of a cylinder with n_{H} of a few 10^6 cm^{-3} , $2''-6''$ length and width of $2''$ is $\lesssim 0.005 M_{\odot}$ (a mass per unit length of $0.3-1.0 M_{\odot} \text{ pc}^{-1}$). This is much lower than the Virial and critical masses [40] needed to make them gravitationally unstable (about $5 M_{\odot}$, from the inferred gas T , n_{H} and velocity dispersion). H_2 clumps of similar small masses (several $0.001 M_{\odot}$) have been intuited towards the boundary of more evolved and distant H II regions [41]. Compression and fragmentation of UV-irradiated cloud edges must be a common phenomenon in the vicinity of young massive stars.

Physical conditions in the ambient molecular cloud

Deeper inside the molecular cloud, $T_{\text{peak}}^{\text{CO } 3-2}$ smoothly decreases from $\sim 170 \text{ K}$ to $\sim 130 \text{ K}$. Therefore, these observations do not suggest temperature spikes at scales of a few arc-seconds. Deeper inside the molecular cloud ($\delta x > 30''$ in our rotated images), both $N(\text{H}_2)$ and $N(\text{HCO}^+)$ are expected to gradually increase [5, 7, 6, 37]. For the expected $N(\text{HCO}^+)\approx 2\times 10^{14} \text{ cm}^{-2}$ column density [5, 6], excitation models show that the gas density in the ambient cloud is $n_{\text{H}}\approx(0.5-1.0)\times 10^5 \text{ cm}^{-3}$ (dashed curves in Extended Data Fig. 3), in agreement with previous estimations [2, 5]. Hence, the over-dense substructures have compression factors $\sim 5-30$ with respect to the ambient molecular gas.

Physical conditions in the atomic layer

The decrease of both $T_{\text{peak}}^{\text{CO } 3-2}$ and $W_{4-3}^{\text{HCO}^+}$ between the ionisation and dissociation fronts is consistent with the expected sharp decrease of CO and HCO^+ abundances in the atomic layer. The representative gas density in the atomic layer, $n_{\text{H}}\approx(4-5)\times 10^4 \text{ cm}^{-3}$, is constrained by the strength of the un-attenuated FUV flux at the Bar edge [5, 3] ($\chi\approx 4.4\times 10^4$, determined by the spectral type of the Trapezium stars) and by the current position of the dissociation front at $\delta x \simeq 15''$ [1, 33]. The exact gas density value, however, depends on the assumed FUV-extinction grain properties (which likely vary as function of cloud depth). In the context of stationary PDR models, larger-than-standard-size grains (lower FUV absorption cross-sections) are often invoked [33], otherwise the separation between the dissociation and ionisation fronts would be smaller than the observed $\sim 15''$. The lower densities in the atomic layer agree with the observed low H_2 $v=1-0$ $S(1)/v=2-1$ $S(1)\approx 3$ line intensity ratio attributed to fluorescent H_2^* excitation [32, 42]. We note that optically thin CO emission implies $T_{\text{peak}}^{\text{CO } 3-2}\ll T_{\text{ex}}$. Hence, $T_{\text{peak}}^{\text{CO } 3-2}$ can no longer be used as a gas thermometer in the atomic layer where the CO abundance is low. The gas temperature close to the dissociation front is between $T\approx 500 \text{ K}$ (from H I observations [13]) and $T\approx 300 \text{ K}$ (from carbon radio-recombination [43] and [C II] $158\mu\text{m}$ [11] line observations).

Emission Probability Distribution Functions (PDF)

In order to study the distribution of gas densities in the region, approximated by the HCO^+ $J=4-3$ emission, we analysed the probability distribution of the logarithmic emission, given by $z=\ln(W_{4-3}^{\text{HCO}^+}/\langle W_{4-3}^{\text{HCO}^+} \rangle)$, where $\langle W_{4-3}^{\text{HCO}^+} \rangle = \langle \int T_B dv \rangle$ is the mean value in the observed FoV (37 K km s^{-1}). This is a common approach to interpret (column) density maps, both from observations and MHD simulations[24, 44]. The PDF is computed as the number of pixels (in the high signal-to-noise $W_{4-3}^{\text{HCO}^+}$ image) per intensity bin divided by the total number of pixels. We first analysed the complete FoV observed by ALMA and selected $W_{4-3}^{\text{HCO}^+}$ measurements above 5 sigma, where we define $\text{sigma} = \text{rms} \cdot (2\delta v \cdot \Delta v_{\text{FWHM}})^{1/2}$, with $\delta v = 0.4 \text{ km s}^{-1}$ and $v_{\text{FWHM}} = 3.0 \text{ km s}^{-1}$. The resulting PDF is shown in Fig. 2d (magenta points). Second, we selected measurements only in the compressed layers region between $\delta x = 7''$ and $30''$ (with respect to the rotated images in Fig. 2). The resulting PDF (black points) is very close to a log-normal distribution with $p(z) = N \exp(-(z - z_0)^2 / 2\sigma^2)$, where z_0 is the peak value and σ the standard deviation. We obtain $z_0 = 0.165$ and $\sigma = 0.31$ from a fit (green curve). If $W_{4-3}^{\text{HCO}^+}$ is proportional to the gas density, these values imply that 99% of the observed positions in the compressed layers span a factor of ~ 6 in density. In MHD models, σ is a measure of how density varies in a turbulent cloud. Hence, it depends on the Mach number, the ratio of the thermal to magnetic pressure (β) and the forcing characteristics of the turbulence[24]. The relatively modest σ value inferred in the $\delta x = 7''$ - $30''$ layer is consistent with the low Mach numbers in the PDR, and suggests a significant role of magnetic pressure. We note that a similar analysis of the CO emission does not yield the same log-normal distribution. This is consistent with low- J CO lines being optically thick and tracing gas temperature and not gas density variations. This reinforces that the log-normal shape of the $W_{4-3}^{\text{HCO}^+}$ PDF in the compressed layer is a relevant observational result.

Gas pressures, magnetic field and compression

To support to the cloud compression and gas photo-ablation scenario, we investigated the different contributions to the gas pressure in the region. The thermal pressure in the H II region near the ionisation front[1] is $P_{\text{th,HII}}/k = 2 \cdot n_e \cdot T_e \approx 6 \times 10^7 \text{ K cm}^{-3}$, about 6 times higher than the turbulent ram pressure $P_{\text{ram,amb}} = \rho \sigma_{\text{nth,amb}}^2$ in the ambient molecular cloud (Extended Data Table 1). Since we find similar contribution of thermal and non-thermal (turbulent) pressures in both the ambient cloud and the over-dense substructures ($\alpha = P_{\text{nth,amb}}/P_{\text{th,amb}} \approx P_{\text{nth,comp}}/P_{\text{th,comp}} \approx 1$), it is reasonable to assume equipartition of thermal, turbulent and magnetic energies to quantify the magnetic pressure in the PDR ($P_B = B^2/8\pi$). In particular, for $\beta = P_B/P_{\text{th}} = 1$ we estimate magnetic fields strengths of $B \approx 200 \mu\text{G}$ and $\approx 800 \mu\text{G}$ in the ambient and in the high-density substructures respectively. Such strong magnetic fields at small scales need to be confirmed observationally (both the strength and the orientation) but seem consistent with the high values ($\sim 100 \mu\text{G}$) mea-

sured in the low-density foreground material[45] (the “Orion Veil”) confirming that B is particularly strong in the Orion complex. On much larger spatial scales, low-angular resolution observations do suggest that B increases with gas density at H II/cloud boundaries ($B \propto n_{\text{H}}^{0.5-1}$)[46].

A strong magnetic field would be associated with large magnetosonic speeds (v_{ms}) in the PDR. If a UV-driven shock-wave is responsible for the molecular gas compression, its velocity is predicted to slow down to $v_{\text{s}} \lesssim 3 \text{ km s}^{-1}$ once entered the molecular cloud[21]. In such a slow, magnetised shock ($v_{\text{s}} \ll v_{\text{ms}}$), compression waves can travel ahead of the shock front[47]. Thus, a high magnetic field strength may be related with the $W_{4-3}^{\text{HCO}^+}$ undulations seen perpendicular to the Bar (Fig. 2c). The inferred compression factor in the observed substructures ($f = n_{\text{comp}}/n_{\text{amb}} = 5-30$) is consistent with slow shock velocities[16], $v_{\text{s}} = c_0 \sqrt{f} \approx 1.5-4.0 \text{ km s}^{-1}$, where c_0 is the initial sound speed of the unperturbed molecular gas. The necessarily small v_{s} agrees with the relatively narrow molecular line-profiles ($\Delta v_{\text{FWHM}} \lesssim 4 \text{ km s}^{-1}$) seen in PDRs[14] (including observations of face-on sources in which the shock would propagate in the line of sight). Owing to the high thermal pressure in the compressed structures, we also find that a pressure gradient, with $P_{\text{th,comp}} \geq P_{\text{th,HII}}$ exists. This subtle effect is seen in simulations of an advancing shock-wave around an H II region[22, 48].

Molecular gas between the ionization and dissociation fronts

ALMA reveals fainter HCO^+ and CO emission in the atomic layer (HCO^+ globulettes and plume-like CO features at $\delta x < 15''$, Fig. 2). Previous low-angular resolution observations and models had suggested the presence of dense spherical clumps with $5''-10''$ sizes deeper inside the molecular cloud[6, 19] (at $\geq 15''-20''$ from the ionisation front[3, 6, 32]). The dense substructures resolved by ALMA are smaller ($\simeq 2'' \times 4''$) and are detected at $\delta x \gtrsim 7''$ (even before the peak of the H_2 vibrational emission).

The molecular line profiles towards the plumes typically show two velocity emission components (Extended Data Fig. 4). One centred at $v_{\text{LSR}} \approx 8.5 \text{ km s}^{-1}$, the velocity of the background molecular cloud in the back-side of M42[11] (not directly associated with the Bar), and other at $v_{\text{LSR}} \approx 11 \text{ km s}^{-1}$, the velocity-component of the molecular gas in the Bar. In addition, despite the small size of the observed region, the crosscuts of the HCO^+ $J=4-3$ line velocity centroid and of the FWHM velocity dispersion, show gradients perpendicular to the Bar (Extended Data Fig. 4). Moving from the ionisation front to the molecular gas, the line centroid shifts to higher velocities (gas compression effects may, in part, contribute to this red-shifted velocity). The velocity dispersion, however, shows its maximum between the ionisation and the dissociation fronts, the expected layers for photoablative neutral gas flows. Both the kinematic association with the Bar velocities and the higher velocity dispersion between the two fronts are consistent with the presence of gas flowing from the high-pressure compressed molecular layers ($P_{\text{th,comp}}/k \approx 2 \times 10^8 \text{ K cm}^{-3}$) to the atomic layers ($P_{\text{th,atomic}}/k \approx 5 \times 10^7 \text{ K cm}^{-3}$).

HCO⁺ chemistry and the C⁺/CO transition zone

Static equilibrium PDR models appropriate to the ambient gas component ($n_{\text{H}} \approx 5 \times 10^4 \text{ cm}^{-3}$) reproduce the separation between the ionisation and dissociation fronts[6]. However, they predict HCO⁺ abundances near the dissociation front that are too low ($x(\text{HCO}^+)$ of a few 5×10^{-11}) to be consistent with the bright ridge of HCO⁺ emission detected by ALMA. These models also predict that the C⁺/CO transition should occur ahead of the H/H₂ transition zone and deeper inside the molecular cloud (at $\delta x \simeq 20''$ from the ionisation front[3, 4]). However, our detection of bright CO and HCO⁺ emission towards the layers of bright H₂ vibrational emission[1] implies that the C⁺/CO transition occurs closer to the cloud edge, and nearly coincides with the H/H₂ transition (at least it cannot be resolved at the $\sim 1''$ resolution of our observations). This is likely another signature of dynamical effects. Indeed, the presence of molecular gas near the cloud edge[49], and a reduced C⁺ abundance deeper inside the molecular cloud[50], may explain model and observation discrepancies of other chemically related molecules. As an example, stationary PDR models applied to the fluorine chemistry[51] overpredict the CF⁺ column density observed towards the Bar[52] by a factor of ~ 10 . Given that HF readily forms as F atoms react with H₂ molecules, CF⁺ must arise from layers where C⁺ and H₂ overlap (CF⁺ forms through $\text{HF} + \text{C}^+ \rightarrow \text{CF}^+ + \text{H}$ reactions and is quickly destroyed by recombination with electrons)[51, 53]. Hence, the (lower-than-predicted) observed CF⁺ abundances likely reflect a dynamical PDR behaviour as well.

Stationary PDR models of strongly irradiated dense gas (with n_{H} of a few 10^6 cm^{-3}) have been presented in the literature[3, 6, 7]. The above densities are similar to those inferred in the compressed substructures at the Bar edge. Thus they can be used to get insights about the chemistry that leads to the formation of HCO⁺ and CO in UV-irradiated dense gas. Owing to the higher densities and enhanced H₂ collisional de-excitation heating, the gas attains high temperatures. This triggers a warm chemistry in which endothermic reactions and reactions with energy barriers become faster. As a result, higher HCO⁺ abundances are predicted close to the dissociation front ($x(\text{HCO}^+)$ of several 10^{-9}). Reactions of C⁺ with H₂ (either far-UV-pumped or thermally excited) initiate the carbon chemistry[54]. This reaction triggers the formation of CH⁺ (explaining the elevated CH⁺ abundances detected by Herschel[55]) and reduces the abundance of C⁺ ions and H₂ molecules near the dissociation front; i.e., the H/H₂ and the C⁺/CO transition layers naturally get closer (in A_{V})[50]. Fast exothermic reactions of CH⁺ with H₂ subsequently produce CH₂⁺ and CH₃⁺. Both hydrocarbon ions are “burnt” in reactions with abundant oxygen atoms and contribute to the HCO⁺ formation at the molecular cloud edge. This HCO⁺ formation route from CH⁺ can dominate over the formation of HCO⁺ from CO⁺ (after the $\text{O} + \text{H}_2 \rightarrow \text{OH} + \text{H}$ reaction, followed by $\text{C}^+ + \text{OH} \rightarrow \text{CO}^+ + \text{H}$, and finally $\text{CO}^+ + \text{H}_2 \rightarrow \text{HCO}^+ + \text{H}$) [5, 6, 32]. Both OH and CO⁺ have been detected in the Bar[56, 57], but high-angular resolution maps do not exist. Recombination of HCO⁺ with electrons then drives CO production near the dissociation front[6, 7].

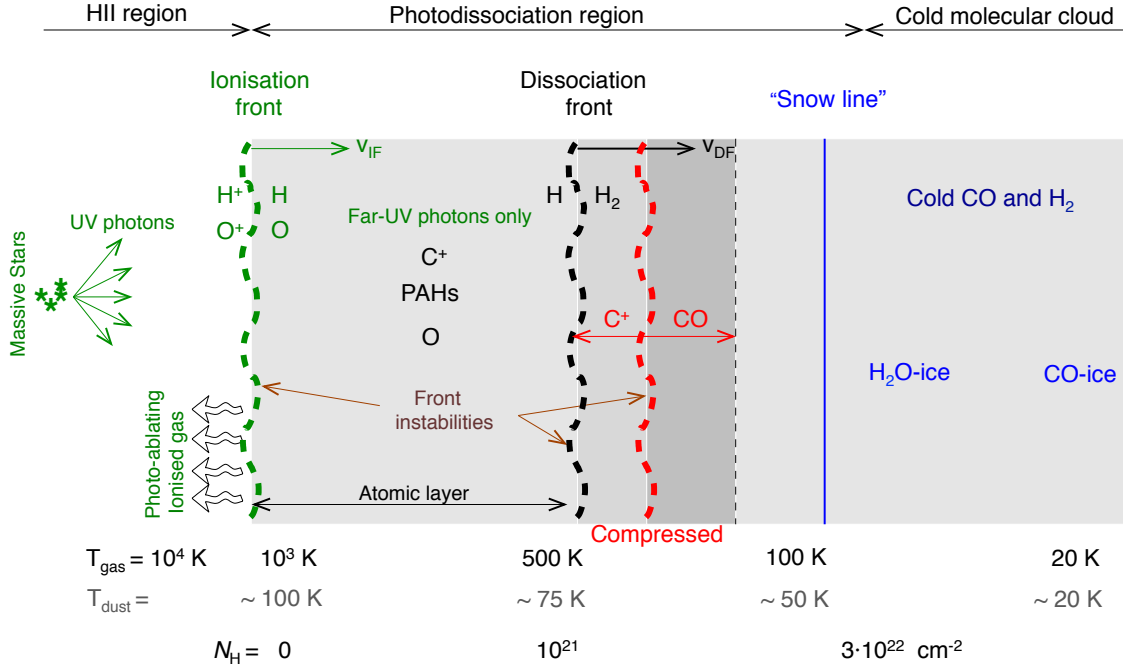
Extrapolating the above chemical scenario, the brightest HCO^+ $J=4-3$ emission peaks in the Bar should be close to H_2^* emission peaks. Extended Data Fig. 2a shows a remarkable spatial agreement between the H_2 $v=1-0$ $S(1)$ emission peaks and several HCO^+ emission peaks. Detailed H_2 excitation models (including both far-UV-pumping and collisions) show that for the conditions prevailing in the Bar, the intensity of the H_2 $v=1-0$ $S(1)$ line is approximately proportional to the gas density[42]. Therefore, the HCO^+ peaks that match the position of the H_2 $v=1-0$ $S(1)$ line peaks likely correspond to gas density enhancements as well. This agrees with the higher H_2 $v=1-0$ $S(1)/v=2-1$ $S(1) \approx 8$ line intensity ratios observed at the dissociation front and consistent with significant H_2 collisional excitation[32]. The ALMA images thus confirm that in addition, or as a consequence of dynamical effects, reactions of H_2 with abundant atoms and ions contribute to shift the molecular gas production towards the cloud edge. Even higher-angular resolution observations of additional tracers will be needed to fully understand this, and to spatially resolve the chemical stratification expected in the overdense substructures themselves. We note that if most carbon becomes CO at $A_V \approx 2$ (N_{H} of a several 10^{21} cm^{-2}) in substructures with gas densities of a few 10^6 cm^{-3} , this depth is equivalent to a spatial length of several 10^{15} cm , or an angular-scale of $\sim 0.5''$ at the distance to Orion.

Deeper inside into the molecular cloud ($\delta x > 30''$), the CO^+ , CH^+ , CH_2^+ and CH_3^+ abundances sharply decrease. The far-UV flux significantly diminishes, and the gas and dust grain temperatures accordingly decrease. The HCO^+ abundance also decreases until the $\text{CO} + \text{H}_3^+ \rightarrow \text{HCO}^+ + \text{H}_2$ reaction starts to drive the HCO^+ formation at low temperatures. Gas-phase atoms and molecules gradually deplete and dust grains become coated by ices as the FUV photon flux is attenuated at even larger cloud depths (see sketch in Extended Data Fig. 1).

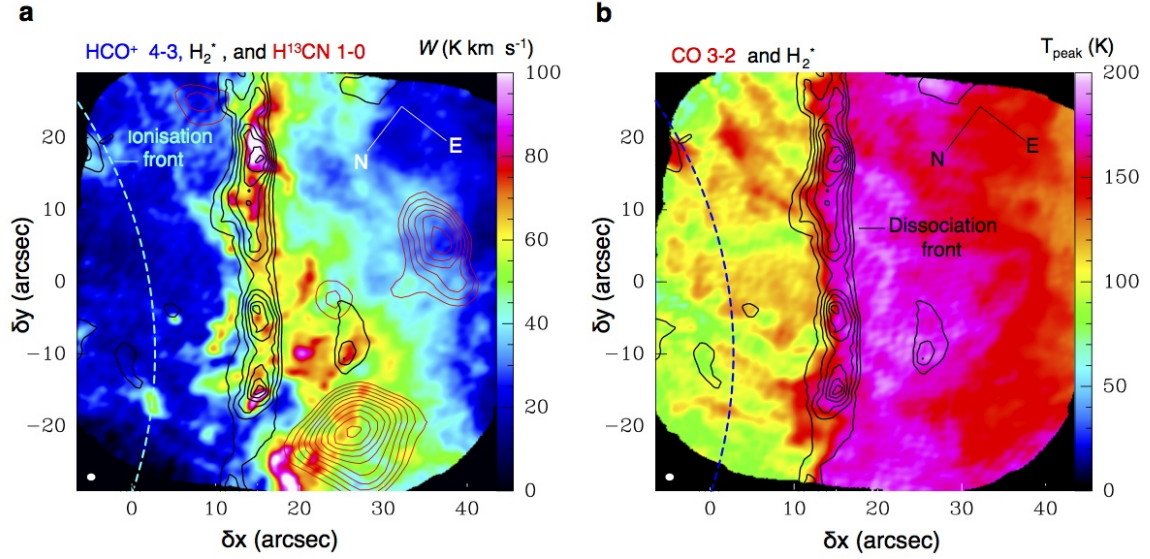
31. Pety, J. & Rodríguez-Fernandez, N. J. Revisiting the theory of interferometric wide-field synthesis. *Astron. Astrophys.* **517**, A12 (2010).
32. van der Werf, P. P., Stutzki, J., Sternberg, A. & Krabbe, A. Structure and chemistry of the Orion bar photon-dominated region. *Astron. Astrophys.* **313**, 633-648 (1996).
33. Allers, K. N., Jaffe, D. T., Lacy, J. H., Draine, B. T. & Richter, M. J. H₂ Pure Rotational Lines in the Orion Bar. *Astrophys. J.* **630**, 368-380 (2005).
34. O'Dell, C. R. & Yusef-Zadeh, F., High Angular Resolution Determination of Extinction in the Orion Nebula. *Astron. J.*, **120**, 382-392 (2000).
35. Cardelli, J. A. Clayton, G. C. & Mathis, J. S. The relationship between infrared, optical, and ultraviolet extinction. *Astrophys. J.* **345**, 245-256 (1989).
36. Goicoechea, J. R. *et al.* Low sulfur depletion in the Horsehead PDR. *Astron. Astrophys.* 456, 565-580 (2006).
37. Arab, H. *et al.* Evolution of dust in the Orion Bar with Herschel. I. Radiative transfer modelling. *Astron. Astrophys.* **541**, A19 (2012).
38. Cuadrado, S. *et al.* The chemistry and spatial distribution of small hydrocarbons in UV-irradiated molecular clouds: the Orion Bar PDR. *Astron. Astrophys.* **575**, A82 (2015).
39. Langer, W. D. & Penzias, A. A. ¹²C/¹³C isotope ratio across the Galaxy from observations of ¹³C¹⁸O in molecular clouds. *Astrophys. J.* **357**, 477-492 (1990).
40. Inutsuka, S.-i. & Miyama, S. M. A Production Mechanism for Clusters of Dense Cores. *Astrophys. J.* **480**, 681-693 (1997).
41. Noel, B. Joblin, C., Maillard, J. P. & Paumard, T. New results on the massive star-forming region S106 by BEAR spectro-imagery. *Astron. Astrophys.* **436**, 569-584 (2005).
42. Burton, M. G., Hollenbach, D. J. & Tielens, A. G. G. M. Line emission from clumpy photodissociation regions. *Astrophys. J.* **365**, 620-639 (1990).
43. Wyrowski, F., Schilke, P., Hofner, P., & Walmsley, C. M. Carbon Radio Recombination Lines in the Orion Bar. *Astrophys. J. Letters.* **487**, L171-L174 (1997).
44. Tremblin, P. *et al.* Ionization compression impact on dense gas distribution and star formation. Probability density functions around H II regions as seen by Herschel. *Astron. Astrophys.* **564**, A106 (2014).

45. Brogan, C. L., Troland, T. H., Abel, N. P., Goss, W. M., & Crutcher, R. M. H I and OH Zeeman Observations Toward Orion's Veil. *Astronomical Polarimetry: Current Status and Future Directions* **343**, 183 (2005).
46. Planck Collaboration, *et al.* Planck intermediate results. XXXIV. The magnetic field structure in the Rosette Nebula. *Astron. Astrophys.* **586**, A137 (2016).
47. Roberge, W. G., & Draine, B. T. A new class of solutions for interstellar magnetohydrodynamic shock waves. *Astrophys. J.* **350**, 700-721(1990).
48. Raga, A. C., Cantó, J., & Rodriguez, L. F. Analytic and numerical models for the expansion of a compact H II region. *MNRAS*. **419**, L39-L43 (2012)
49. Hollenbach, D. J. & Natta, A. Time-Dependent Photodissociation Regions. *Astrophys. J.* **455**, 133-144 (1995).
50. Bertoldi, F. ISO: A Novel Look at the Photodissociated Surfaces of Molecular Clouds. *ESA Special Publication* **419**, 67-72 (1997).
51. Neufeld, D. A. & Wolfire, M. G. The Chemistry of Interstellar Molecules Containing the Halogen Elements. *Astrophys. J.* **706**, 1594-1604 (2009).
52. Neufeld, D. A. *et al.* Discovery of interstellar CF^+ . *Astron. Astrophys.* **454**, L37-L40 (2006).
53. Guzmán, V. *et al.* The IRAM-30m line survey of the Horsehead PDR. I. CF^+ as a tracer of C^+ and as a measure of the fluorine abundance. *Astron. Astrophys.* **443**, L1 (2012).
54. Agúndez, M., Goicoechea, J. R., Cernicharo, J., Faure, A. & Roueff, E. The Chemistry of Vibrationally Excited H_2 in the Interstellar Medium. *Astrophys. J.* **713**, 662-670 (2010).
55. Nagy, Z. *et al.* The chemistry of ions in the Orion Bar I. - CH^+ , SH^+ , and CF^+ . The effect of high electron density and vibrationally excited H_2 in a warm PDR surface. *Astron. Astrophys.* **550**, A96 (2013).
56. Goicoechea, J. R. *et al.* OH emission from warm and dense gas in the Orion Bar PDR. *Astron. Astrophys.* **530**, L16 (2011).
57. Stoerzer, H., Stutzki, J. & Sternberg, A. CO^+ in the Orion Bar, M17 and S140 star-forming regions. *Astron. Astrophys.* **296**, L9-L12 (1995).

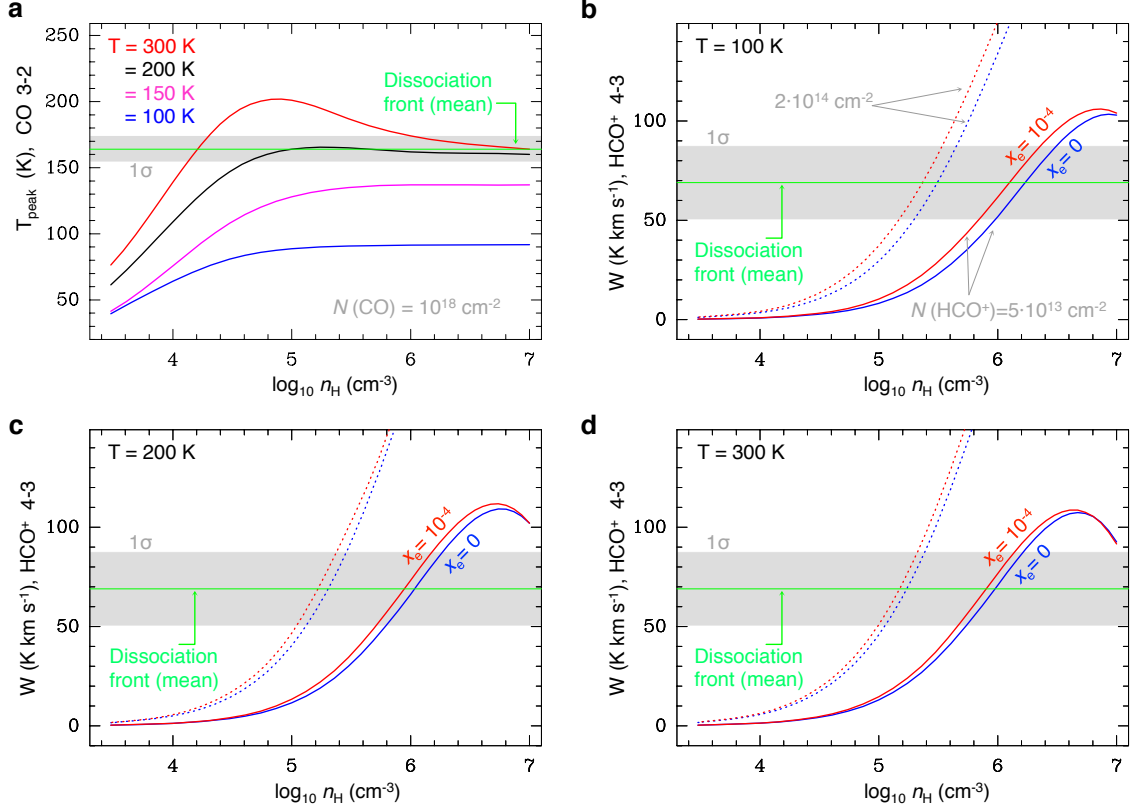
Extended Data



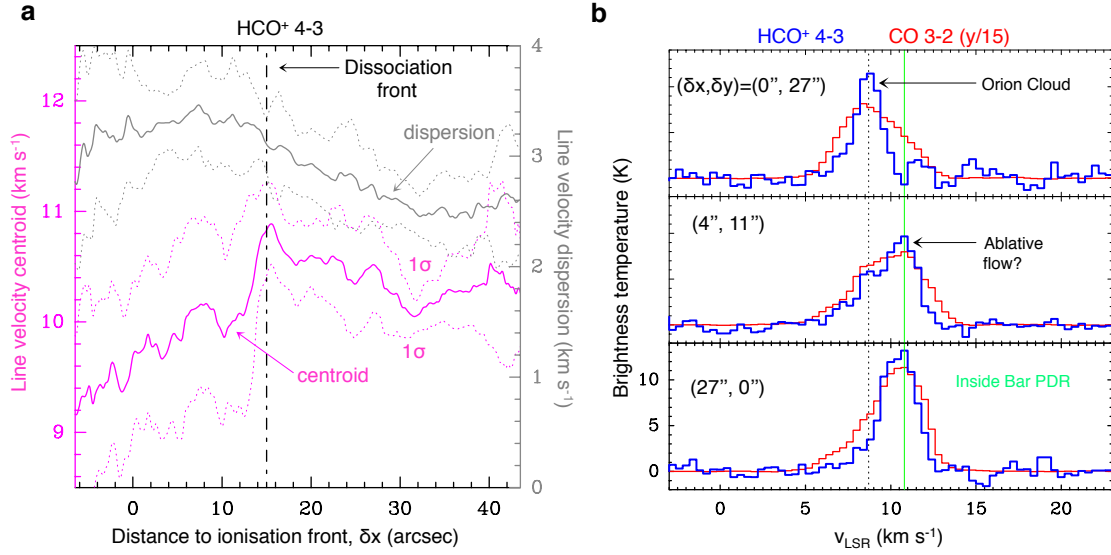
Extended Data Figure 1: Structure of a strongly UV-irradiated molecular cloud edge. The incident stellar UV radiation comes from the left. The velocity of the advancing ionisation and dissociation fronts are represented by v_{IF} and v_{DF} respectively. In the Orion Bar, the dissociation front is at about $15''$ ($\sim 0.03 \text{ pc}$) from the ionisation front.



Extended Data Figure 2: Comparison with other tracers. **a**, ALMA HCO^+ $J=4-3$ line integrated intensity, **b**, ALMA CO $J=3-2$ line peak (Bar velocity component). The red contours represent the H^{13}CN $J=1-0$ emission (from 0.08 to 0.026 by 0.02 $\text{Jy beam}^{-1} \text{ km s}^{-1}$) of dense condensations inside the Bar [19]. The black contours show the brightest regions of H_2 $v=1-0$ $S(1)$ emission[1] (from 1.5 to 4.5 by $0.5 \times 10^{-4} \text{ erg s}^{-1} \text{ cm}^{-2} \text{ sr}^{-1}$). The H_2^* image is saturated between $\delta x=19''$ and $23''$ (i.e. no data is shown). Figures have been rotated by 127.5° anticlockwise to bring the incident UV radiation from left.



Extended Data Figure 3: Excitation models for different gas temperatures and densities. **a**, CO $J=3-2$ line peak (for $N(\text{CO})=10^{18} \text{ cm}^{-2}$). **b**, **c** and **d** HCO $^{+}$ $J=4-3$ integrated line intensity. Each curve represents a different electron abundance model: $x_e=0$ (blue) and 10^{-4} (red). Continuous curves are for $N(\text{HCO}^{+})=5 \times 10^{13} \text{ cm}^{-2}$ and dotted lines for $N(\text{HCO}^{+})=2 \times 10^{14} \text{ cm}^{-2}$ (appropriate for deeper inside the Bar, $\delta x > 30''$). The horizontal green dashed line represents the average $T_{\text{peak}}^{\text{CO } 3-2}$ (**a**) and $W_{4-3}^{\text{HCO}^{+}}$ (**b**, **c**, and **d**) with their standard deviation (grey shaded) towards the dissociation front (at $\delta x \approx 15''$).



Extended Data Figure 4: Line velocity centroid, dispersion and profiles.

a, Vertically-averaged cuts perpendicular to the Bar in the HCO⁺ $J=4-3$ line velocity centroid (magenta curve) and FWHM velocity dispersion (grey curve). **b**, CO and HCO⁺ spectra at representative positions. The first two panels (from top to bottom) are positions between the ionisation and dissociation fronts, the third one is inside the molecular Bar. Offsets are given with respect to the rotated images in Extended Data Fig. 2. The velocity of the background cloud is $v_{\text{LSR}} \approx 8.5 \text{ km s}^{-1}$ (black dashed line), whereas the velocity of the Bar is $v_{\text{LSR}} \approx 11 \text{ km s}^{-1}$ (green line).

	Ionisation front	Atomic layer	Compressed structures	Ambient PDR component
Thermal pressure (K cm ⁻³)	$P_{\text{th,HII}}/k \approx 6 \cdot 10^7$	$P_{\text{th,HII}}/k \leq 5 \cdot 10^7$	$P_{\text{th,comp}}/k \approx 2 \cdot 10^8$	$P_{\text{th,amb}}/k \approx 10^7$
Non-thermal pressure* (K cm ⁻³)			$P_{\text{nth,comp}}/k \approx 2 \cdot 10^8$	$P_{\text{nth,amb}}/k \approx 10^7$
Magnetic field B (for $\beta=P_B/P_{\text{th}}=1$)			$\approx 800 \text{ } \mu\text{Gauss}$	$\approx 200 \text{ } \mu\text{Gauss}$

Extended Data Table 1: Gas pressures and estimated magnetic field strengths.
All values are for a non-thermal velocity dispersion of $\sigma_{\text{nth}} \approx 1 \text{ km s}^{-1}$.